

Magnetic Friedel Oscillation at the Fe(001) Surface: Direct Observation by Atomic-Layer-Resolved Synchrotron Radiation ^{57}Fe Mössbauer Spectroscopy

T. Mitsui^{1,2,*}, S. Sakai², S. Li², T. Ueno^{1,2}, T. Watanuki^{1,2}, Y. Kobayashi,³
R. Masuda⁴, M. Seto,^{1,3} and H. Akai⁵

¹National Institutes for Quantum and Radiological Science and Technology, Sayo, Hyogo 679-5148, Japan

²National Institutes for Quantum and Radiological Science and Technology, Takasaki, Gunma 370-1292, Japan

³Institute for Integrated Radiation and Nuclear Science, Kyoto University, Asashironishi, Kumatori, Osaka 590-0494, Japan

⁴Faculty of Science and Technology, Hirosaki University, Bunkyocho, Hirosaki, Aomori 036-8152, Japan

⁵The Institute for Solid State Physics, The University of Tokyo, Kashiwa, Chiba 277-8581, Japan



(Received 9 February 2020; revised 13 July 2020; accepted 16 October 2020; published 3 December 2020)

The surface magnetism of Fe(001) was studied in an atomic layer-by-layer fashion by using the *in situ* iron-57 probe layer method with a synchrotron Mössbauer source. The observed internal hyperfine field H_{int} exhibits a marked decrease at the surface and an oscillatory behavior with increasing depth in the individual upper four layers below the surface. The calculated layer-depth dependencies of the effective hyperfine field $|H_{\text{eff}}|$, isomer shift δ , and quadrupole shift 2ϵ agree well with the observed experimental parameters. These results provide the first experimental evidence for the magnetic Friedel oscillations, which penetrate several layers from the Fe(001) surface.

DOI: 10.1103/PhysRevLett.125.236806

A knowledge of the surface and interface magnetism of 3d transition metals is of interest due to the essential role that magnetism plays in determining magnetic interactions and spin-transport properties of nanomagnets and magnetic heterojunctions. Over the past few decades, various techniques have advanced studies on surface and interface magnetism [1–4]. However, few experimental studies have investigated the depth-dependent local magnetic structures of surfaces and interfaces on the atomic layer level. This situation is due to the difficulties encountered when performing depth-resolved investigations at the uppermost surface of a metal, e.g., with scanning tunneling microscopy, or due to the signal arising from a relatively broad range of depth, e.g., with x-ray magnetic circular dichroism spectroscopy. One potential approach to study depth-resolved magnetism at surfaces and interfaces is through the use of Mössbauer spectroscopy with isotope probe atoms. In this method, a resonant isotope probe layer is embedded in a film prepared with the nonresonant isotope. The hyperfine parameters derived from the resulting spectrum facilitate depth-resolved analysis of the magnetic interactions in a single atomic layer [5,6]. The observed internal magnetic hyperfine field H_{int} at the nucleus provides details about the local surface magnetism. Furthermore, isomer shifts and quadrupole interactions provide information on the *s*-electron density and electric-field gradient at the nucleus, respectively.

Surface magnetism of Fe(001) is a fascinating research subject for atomic-layer-resolved magnetic analysis. Theoretical calculations predict 30% enhancement of the magnetic moment M_{Fe} at the surface and an oscillatory

behavior with increasing depth in the individual layers, i.e., a magnetic Friedel oscillation [7,8]. As a relevant phenomenon, Ohnishi, Freeman, and Weinert theoretically predicted that H_{int} is reduced by 30% relative to the bulk value despite a significant increase in the surface M_{Fe} [9]. Experimentally, Kiauka *et al.* studied the surface magnetism of Fe(001) using *in situ* conversion electron Mössbauer spectroscopy with iron-57 as a probe layer [10]. However, conventional Mössbauer spectroscopy with a cobalt-57 source requires a measurement time longer than several weeks. Hence, sample surface contamination from residual gas cannot be avoided even under ultrahigh vacuum conditions. Consequently, they could not detect the drastic changes of H_{int} predicted for the clean Fe(001) surface. To date, the surface magnetism of iron remains unclear, particularly its variation toward the bulk region.

High-brilliance synchrotron radiation has greatly improved the iron-57 probe layer method. Early studies employed nuclear resonance forward scattering, which records time-domain Mössbauer spectra, to perform advanced surface studies [11–14]. Today, synchrotron Mössbauer sources can be used to observe energy domain spectra [15–18]. The modern method can rapidly measure the absorption spectrum of the iron-57 probe for one monolayer (ML) embedded in the film surface using the total reflection of iron-57 Mössbauer γ rays filtered from synchrotron radiation [17].

In this study, the layer-by-layer hyperfine parameters of the Fe(001) surface are determined by the *in situ* iron-57 probe layer method with a synchrotron Mössbauer source. Additionally, the surface magnetism is discussed by comparing experimental results with *ab initio* calculations.

In situ synchrotron studies were performed in a special measurement chamber, which was equipped with a liquid helium flow cryostat and electromagnetic coils. The chamber had a base pressure below 2×10^{-9} Pa and was connected to a molecular beam epitaxy chamber with a base pressure of 2×10^{-8} Pa for sample preparation. The layer-by-layer hyperfine interactions were immediately observed in this combined ultrahigh vacuum system by transferring the samples from the molecular-beam epitaxy chamber to the measurement chamber without breaking the ultrahigh vacuum.

Fe(001) films were fabricated by alternatively evaporating iron-56 and iron-57 from 99.94% iron-56 and 95.93% iron-57 isotopic sources onto precleaned $10 \times 10 \times 0.5$ mm³ MgO(001) substrates under a vacuum pressure of approximately 10^{-8} Pa (Supplemental Fig. S1 [19]). A 0.8-ML-thick iron-57 probe layer, $t = 0.1$ nm, was embedded to the depth of the N th atomic layer, $N = 1-4$ and 7, below the surface. These samples are hereafter referred to as “ N th probe layer samples.”

All samples were prepared according to the following recipe. An iron-56 (001) layer with a 4.0–4.9 nm thickness was deposited on MgO(001) at a substrate temperature of 473 K. Then, 0.8 ML of the iron-57 probe layer and 0–6 ML of the iron-56 were deposited at 300 K to minimize atomic intermixing [10]. The total film thickness was monitored by a quartz crystal microbalance and fixed to 5.0 nm in all samples. The *in situ* reflection high-energy electron diffraction pattern revealed that all samples exhibited body-centered cubic iron film growth with an Fe(001)[100]//MgO(001)[110] epitaxial relation. Streaky patterns with intense specular spots suggested a flat iron surface with (001) terraces created by two-dimensional growth [20]. This observation was also supported by *ex situ* atomic force microscopy (Supplemental Fig. S2 [19]).

The experiments were performed at BL11XU of SPring-8 using linearly π -polarized 14.4 keV Mössbauer γ rays with a 15.4 neV bandwidth produced by a synchrotron Mössbauer source [16]. The γ -ray beam was vertically focused by an elliptical mirror. The beam size was $15 \mu\text{m}$ (V) \times 1.6 mm (H), and the beam flux was about 2.9×10^4 photons/s. This beam was introduced into the measurement chamber to perform grazing incidence measurements [Fig. 1(a)]. An external magnetic field of 300 Oe was applied antiparallel to the beam direction to magnetize the Fe(001) film along the in-plane [110] easy axis. In this arrangement, the π -polarized incident beam interacted with the four nuclear transitions of $\Delta m = \pm 1$. The Mössbauer absorption spectra were measured by collecting the totally reflected γ rays from the sample surface at an incident angle of 0.1° with a reflectivity of about 80% [17]. Each spectrum was obtained within a few hours of sample preparation. Such short-time measurements significantly reduced the

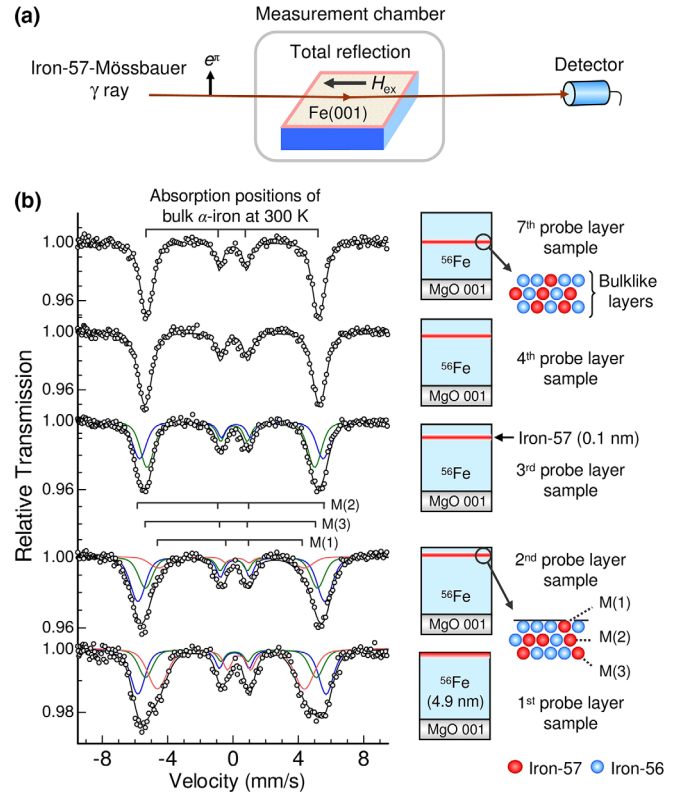


FIG. 1. (a) Experimental setup. e_x , electric field vector of the incident beam; H_{ex} , external magnetic field (300 Oe); detector, NaI(Tl) scintillation detector. (b) Mössbauer spectra of the N th probe layer samples measured at 300 K. Black solid lines represent the fitted curves. Red, blue, and green lines represent three different magnetic components. $M(i)$ represents the magnetic component assigned to the iron-57 atoms located in the i th layer below the surface.

residual gas absorption and oxidation on the Fe(001) surfaces [21,22] (Supplemental Fig. S3 [19]).

Figure 1(b) presents the Mössbauer spectra of the N th probe layer samples, $N = 1-4$ and 7, recorded at 300 K. All samples showed magnetically split Mössbauer patterns. The isomer shift δ relative to room-temperature α -iron, quadrupole shift 2ϵ , and hyperfine field H_{int} were derived from the four-line spectrum using the method proposed by Zemčík [23]. Because the broadened absorption lines imply a small magnetic distribution, the spectra were analyzed using the Voigt function, i.e., a convolution of the Lorentzian and Gaussian [24]. The Lorentz linewidth was 0.47 mm/s based on the measurement of a natural α -iron film (Supplemental Fig. S4 [19]), while the Gaussian linewidth represented the width of the H_{int} distribution ΔH_{int} . Table I summarizes the analysis results.

The spectra of the first, second, and third probe layer samples exhibited complex profiles composed of different magnetic components, i.e., small H_{int} (red lines, around 28 T), large H_{int} (blue lines, around 36 T), and bulklike H_{int} (green lines, around 32 T) [Fig. 1(b)]. The small H_{int} is not

TABLE I. Experimental hyperfine parameters for the N th probe layer samples at 300 K.

N	$M(i)^a$	A^b (%)	H_{int} (T)	δ (mm/s)	2ϵ (mm/s)	ΔH_{int} (T)
1	$M(1)^*$	40	28.0(5)	0.12(3)	-0.50(6)	6.6(8)
	$M(2)$	37	35.8(5)	0.06(5)	-0.14(10)	4.5(9)
	$M(3)$	23	32.5(6)	-0.02(8)	-0.21(16)	4.3(4)
2	$M(1)$	15	27.7(2)	0.09(10)	-0.38(19)	6.1(18)
	$M(2)^*$	51	35.6(2)	0.01(2)	-0.23(4)	4.8 (6)
	$M(3)$	34	32.7(5)	-0.03(4)	-0.14(8)	4.3(6)
3	$M(2)$	45	35.0(1)	0.04(1)	-0.28(3)	4.2(4)
	$M(3)^*$	55	31.9(1)	-0.03(1)	-0.19(2)	4.1(3)
4	$M(4)$	100	33.20(3)	0.01(1)	-0.11(1)	4.2(1)
7	$M(7)$	100	32.7(1)	-0.01(1)	-0.02(3)	3.8(2)

^a $M(i)$ represents the magnetic component assigned to the iron-57 atoms located in the i th atomic layer below the surface. An asterisk denotes the prominent component of the N th probe layer sample.

^b A is the area percentage of the $M(i)$ component.

due to thermal effects, because the low-temperature experiment provided almost the same results as those at 300 K (Supplemental Fig. S5 and Table SI [19]). Each sample exhibited different area percentage values for the three components. The values depended on the embedded depth of the iron-57 probe layer. The small H_{int} , large H_{int} , and bulklike H_{int} components were maximized in the first, second, and third probe layer samples, respectively. Furthermore, as the embedding position of the iron-57 probe layer became deeper, the bulklike H_{int} component increased, while the small H_{int} component decreased.

The ideal probe layer in the sample was surrounded by finely distributed iron-57 atoms, which stemmed from the random deposition and surface diffusion of iron atoms during the growth process. Figure 1(b) (right) shows a conceptual diagram. In this case, if the first, second, and third layers of the iron surface have different H_{int} values, the spectra should exhibit a complex profile with multiple components. Based on the systematic behavior of the three components, the small H_{int} , large H_{int} , and bulklike H_{int} represented the intrinsic hyperfine fields for the first, second, and third layers from the surface, respectively. In contrast, the spectra of the fourth and seventh probe layer samples exhibited a single magnetic component with four absorption lines, even in the presence of finely distributed iron-57 atoms. This is because the hyperfine fields of the neighboring layers at these depth regions are bulklike, and the overlapping subspectra result in a simple absorption profile. The prominent subspectrum with the largest percent area in the N th probe layer sample was assigned to the spectrum characterizing the iron-57 atoms located in the N th atomic layer from the surface.

Figures 2(a) and 2(b) plot the layer-by-layer hyperfine parameters derived from the prominent subspectra in

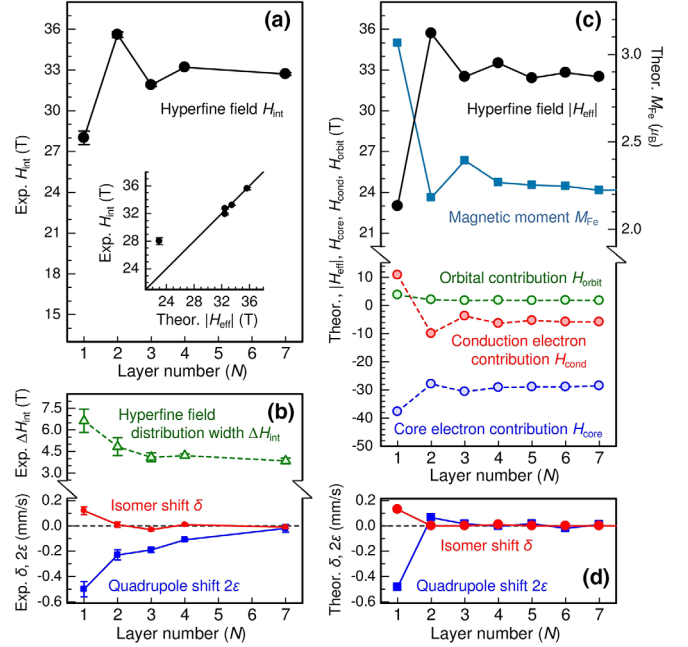


FIG. 2. Plots of the experimental and theoretical layer-by-layer hyperfine parameters. (a) Experimental H_{int} values and experimental H_{int} vs theoretical $|H_{\text{eff}}|$ values. (b) Experimental δ , 2ϵ , and ΔH_{int} values. (c) Theoretical M_{Fe} , $|H_{\text{eff}}|$, H_{core} , H_{cond} , and H_{orbit} values. (d) Theoretical δ and 2ϵ values. Circles and symbols denote data points. Solid and dashed lines connect data points. In (a) and (b), some uncertainties are less than the size of the data points.

the N th probe layer samples. For comparison, Figs. 2(c) and 2(d) show the theoretically calculated layer-by-layer M_{Fe} and hyperfine parameters for a 30-ML-thick Fe(001) film, respectively. Table II summarizes the values.

In the theoretical calculations, M_{Fe} , effective hyperfine field H_{eff} , and δ were calculated using the local density approximation combined with the optimized effective potential method using the exact exchange potential for core states [25,26].

H_{eff} , whose absolute value corresponds to the experimental H_{int} , was calculated as the sum of the contributions of the relativistically corrected Fermi contact interaction [25]

TABLE II Theoretical layer-by-layer magnetic moment and hyperfine parameters of a 30-ML-thick Fe(001) film.

N^a	1	2	3	4	5	6	7	15
$M_{\text{Fe}} (\mu_B)$	3.07	2.18	2.39	2.27	2.25	2.25	2.22	2.24
H_{eff} (T)	-23.0	-35.7	-32.5	-33.5	-32.4	-32.8	-32.5	-32.5
H_{core} (T)	-37.7	-27.9	-30.6	-29.1	-28.9	-28.9	-28.5	-28.8
H_{cond} (T)	10.9	-9.9	-3.7	-6.3	-5.3	-5.8	-5.8	-5.6
H_{orbit} (T)	3.8	2.1	1.8	1.9	1.8	1.9	1.8	1.9
δ (mm/s)	0.13	0.00	0.00	0.01	0.00	0.00	0.00	0.00
2ϵ (mm/s)	-0.48	0.07	0.02	0.00	0.01	-0.02	0.01	0.00

^a N is the number of individual atomic layer from the surface.

and the unquenched orbital angular momentum H_{orbit} . The relativistic contact term is nonlocal, and the electron spins are averaged over a sphere with a radius of Zr_e , where Z and r_e are the atomic number and classical electron radius, respectively. This treatment corrected the inaccuracy of calculations using the classical Fermi contact interaction [25]. The contact interaction, which is the dominant contribution to H_{eff} at the nucleus, is composed of the contributions of the 1s, 2s, and 3s core electrons H_{core} and 4s conduction electrons H_{cond} [Fig. 2(c)].

A factor $\alpha = -0.24a_0^3$ mm/s was used for the calibration of the isomer shift through the expression $\delta = \alpha\rho(0)$, where a_0 is the Bohr radius and $\rho(0)$ is the difference in electron probability density at iron-57 nuclei between the sample studied and isomer shift reference material, i.e., bulk α -iron [25].

The value of 2ε was calculated based on the electric-field gradient derived from the full-potential Korringa-Kohn-Rostoker method [27]. In the measured Fe(001) films, the magnetic interactions were much larger than quadrupole interactions. Although spin-orbit coupling had a small effect under magnetization along the [110] direction, the calculated asymmetry parameter of the electric-field-gradient tensor was negligible based on the virtually preserved tetragonal symmetry with respect to the surface normal. Therefore, the quadrupole shift 2ε is related to the iron-57 experimental nuclear excited state quadrupole moment Q , which is 0.16 b [28], the principal component of the electric-field gradient V_{zz} , and the angle θ between H_{int} and the direction of V_{zz} as $2\varepsilon = eQV_{zz} \times (3 \cos^2\theta - 1)/4$. Because V_{zz} is parallel to [001], the angle θ is 90° and $2\varepsilon = -eQV_{zz}/4$.

Experiments and calculations provided important insights into the hyperfine field at and near the Fe(001) surface. The experimentally observed layer-by-layer H_{int} exhibited a marked decrease at the surface and an oscillatory decay toward the bulk value [Fig. 2(a)]. This behavior was successfully reproduced by theoretical calculations, except for a difference larger than the experimental uncertainty at the surface [Fig. 2(c)]. Theoretically, the oscillatory decay of H_{int} is strongly coupled with the Friedel oscillation of M_{Fe} , as discussed below.

The H_{core} of -28.5 T for bulk iron generally provides a large negative contribution, which opposes the magnetic moment direction, and its absolute value scales with the local M_{Fe} . In contrast, H_{cond} consists of a negative indirect spin polarization due to s - d hybridization with neighboring iron atoms and a positive spin polarization caused by intra-atomic direct s - d exchange interactions. In bulk iron, the negative indirect polarization is dominant. Thus, H_{cond} had the same sign as H_{core} , e.g., $H_{\text{cond}} = -5.8$ T for $N = 7$. However, at the iron surface, the low-coordinated surface atoms reduced the negative indirect polarization, whereas the large M_{Fe} of $3.07\mu_B$ enhanced the positive direct polarization, resulting in a large positive contribution

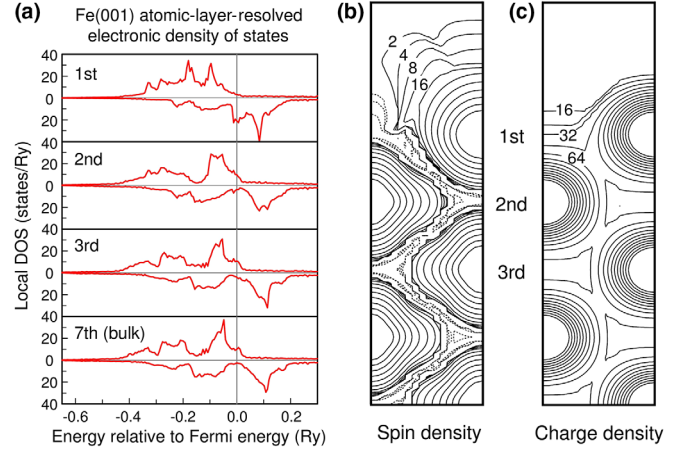


FIG. 3. Band structures and surface states of a 30-ML-thick Fe(001) film. (a) Layer-resolved electron density of states. (b) Spin density map in units of 10^{-4} electrons/ a_0^3 on the (110) plane. Each contour differs by a factor of 2. Dashed lines indicate a negative spin density. (c) Charge density map in units of 10^{-3} electrons/ a_0^3 on the (110) plane. Each contour differs by a factor of $\sqrt{2}$. In (b), the dashed contours between the atoms exhibit a Friedel-type oscillation penetrating the surface.

$H_{\text{cond}} = 10.9$ T. Furthermore, the low symmetry of iron arrangements and the large M_{Fe} at the surface enhanced the positive orbital contribution $H_{\text{orbit}} = 3.8$ T and negative core electron contribution $H_{\text{core}} = -37.7$ T, respectively. Therefore, the absolute value of the effective hyperfine field, $|H_{\text{eff}}| = |H_{\text{core}} + H_{\text{cond}} + H_{\text{orbit}}|$, was reduced by 9.5 T compared to the bulk. Meanwhile, in the second layer, atoms with a small M_{Fe} of $2.18\mu_B$ reduced the positive direct polarization, whereas the iron atoms in the first layer with a large M_{Fe} enhanced the negative indirect polarization. Consequently, H_{cond} had a large negative contribution of -9.9 T. Here, the orbital and core electron contributions were comparable to those for bulk iron, i.e., $H_{\text{orbit}} = 2.1$ T and $H_{\text{core}} = -27.9$ T, respectively. Compared to the bulk, $|H_{\text{eff}}|$ was increased by 3.2 T. When repeating this process, $|H_{\text{eff}}|$ oscillated inversely to the Friedel oscillation of M_{Fe} . Therefore, the experimentally observed H_{int} oscillations penetrating the Fe(001) surface provide direct evidence of a magnetic Friedel oscillation caused by the surface electronic structure with a large spin imbalance and d -band narrowing [Fig. 3(a)].

The difference in H_{int} at the surface between the experimental and theoretical results was unresolved, because the calculations did not consider the existence of surface defects on the measured iron films (Supplemental Fig. S2 [19]). Surface defects were inferred from ΔH_{int} increasing toward the surface, which may be related to the locally modified magnetism at the surface caused by changes in the coordination number due to surface defects, e.g., edges, steps, kinks, and vacancies [29–31]. To elucidate the extrinsic effects, calculations that consider surface defects and more refined experiments are essential.

The theoretical calculations predicted other significant changes in the hyperfine interactions, which are associated with the surface discontinuity. δ showed a large increase, while 2ε showed a sharp decrease [Fig. 2(d)]. The former is attributed to the decreased charge density at the surface, while the latter is induced by a discontinuous distribution of the surface charge density. Unlike the surface spin density [Fig. 3(b)], the surface charge density was already bulklike structure at one atomic layer below the surface [Fig. 3(c)]. This is because Coulomb interactions screen the charge density, but such a mechanism does not exist for the spin density. The charge density variation at the Fe(001) surface was quantitatively confirmed by our experiments. The measured δ increased significantly in the first layer but decreased to around zero in deeper regions, $N = 2-4$ and 7 [Fig. 2(b)]. These observations are consistent with the theoretical results. Note that the measured isomer shift at the Fe(001) surface, $\delta = 0.12$ mm/s, was approximately twice the value reported for the Fe(110) surface [32]. This difference is attributed to the fact that the Fe(001) surface is more open than the Fe(110) surface, which is theoretically predicted not to exhibit a magnetic Friedel oscillation [33]. The measured 2ε data exhibited a large negative value in the first layer [Fig. 2(b)]. The value became less negative as N increased from 2 to 4 and eventually reached zero for $N = 7$. The large negative value at the surface is consistent with the theoretical value, reflecting the broken translational symmetry at the surface. However, the calculations assuming an ideal Fe(001) surface could not reproduce the small negative values in the subsurface. Hence, the small negative values are inferred to be related to the slight lattice distortion near the surface caused by surface defects [34].

In summary, the layer-by-layer hyperfine interactions on the Fe(001) surface observed by synchrotron Mössbauer spectroscopy revealed that the magnetic Friedel oscillations penetrate deep into the fourth sublayer. On the other hand, the charge density is recovered into the bulklike structure at one atomic layer below the surface. In the future, the *in situ* iron-57 probe layer method with a synchrotron Mössbauer source should facilitate additional studies on the surface and interface magnetism in advanced magnetic and spintronic materials and devices.

The authors thank Professor K. Mibu, Professor Y. Yamada, Dr. H. Naramoto, Dr. S. Entani, Dr. T. Inami, and Dr. Y. Katayama for their helpful discussions. This work was carried out at SPring-8 (Proposals No. 2017A3551, No. B3551, No. 2018A3552, No. B3551, No. B3552, and No. 2019A3551) and was partially supported by a Grant-in-Aid for Scientific Research (Grants No. 16H03875, No. 17H07376, No. 17K18373, and No. 18K13985) from the Japan Society for the Promotion of Science.

T. M. and S. S. designed the study and wrote the initial draft of the manuscript. S. L., T. U., Y. K., and R. M. contributed to the sample preparation and data collection. M. S. and T. W. contributed to the analysis, interpretation

of the data, and critically reviewed the manuscript. H. A. contributed to the theoretical calculations and interpretations. All authors have approved the final version of the manuscript and agree to be accountable for all aspects of this work to ensure that questions related to the accuracy or integrity of any part of the work are appropriately investigated and resolved.

*taka@spring8.or.jp

- [1] A. Tange, C. L. Gao, B. Yu, Yavorsky, I. V. Maznichenko, C. Etz, A. Ernst, W. Hergert, I. Mertig, W. Wulfhekel, and J. Kirschner, *Phys. Rev. B* **81**, 195410 (2010).
- [2] U. Gradmann, G. Waller, R. Feder, and E. Tamura, *J. Magn. Magn. Mater.* **31-34**, 883 (1983).
- [3] Y. Yamauchi and M. Kurahashi, *Appl. Surf. Sci.* **169-170**, 236 (2001).
- [4] K. Amemiya, *Phys. Chem. Chem. Phys.* **14**, 10477 (2012).
- [5] T. Shinjo, *Surf. Sci. Rep.* **12**, 51 (1991).
- [6] W. Keune, *Hyperfine Interact.* **204**, 13 (2012).
- [7] C. S. Wang and A. J. Freeman, *Phys. Rev. B* **24**, 4364 (1981).
- [8] A. J. Freeman, H. Krakauer, S. Ohnishi, D. S. Wang, M. Weinert, and E. Wimmer, *J. Phys. J. Phys (Paris). Colloq.* **43**, C7-167 (1982).
- [9] S. Ohnishi, A. J. Freeman, and M. Weinert, *Phys. Rev. B* **28**, 6741 (1983).
- [10] W. Kiauka, K. Debusmann, W. Keune, R. A. Brand, N. Hosoi, and D. Liljequist, *Solid State Commun.* **58**, 641 (1986).
- [11] L. Niesen, A. Mugarza, M. F. Rosu, R. Coehoorn, R. M. Jungblut, F. Roozeboom, A. Q. R. Baron, A. I. Chumakov, and R. Rüffer, *Phys. Rev. B* **58**, 8590 (1998).
- [12] R. Röhlberger, H. Thomas, K. Schlage, E. Burkel, O. Leupold, and R. Rüffer, *Phys. Rev. Lett.* **89**, 237201 (2002).
- [13] K. Schlage, R. Röhlberger, T. Klein, E. Burkel, C. Strohm, and R. Rüffer, *New J. Phys.* **11**, 013043 (2009).
- [14] S. Couet, T. Diederich, S. Stankov, K. Schlage, T. Slezak, R. Rüffer, J. Korecki, and R. Röhlberger, *Appl. Phys. Lett.* **94**, 162501 (2009).
- [15] G. V. Smirnov, U. van Bürck, A. I. Chumakov, A. Q. R. Baron, and R. Rüffer, *Phys. Rev. B* **55**, 5811 (1997).
- [16] T. Mitsui, N. Hirao, Y. Ohishi, R. Masuda, Y. Nakamura, H. Enoki, K. Sakaki, and M. Seto, *J. Synchrotron Radiat.* **16**, 723 (2009).
- [17] T. Mitsui, R. Masuda, M. Seto, E. Suharyadi, and K. Mibu, *J. Synchrotron Radiat.* **19**, 198 (2012).
- [18] T. Mitsui, Y. Imai, R. Masuda, M. Seto, and K. Mibu, *J. Synchrotron Radiat.* **22**, 427 (2015).
- [19] See Supplemental Material at <http://link.aps.org/supplemental/10.1103/PhysRevLett.125.236806> for additional experimental data, the detailed results of sample characterization, and Mössbauer measurements.
- [20] P. Torelli, S. Benedetti, P. Luches, L. Gragnaniello, J. Fujii, and S. Valeri, *Phys. Rev. B* **79**, 035408 (2009).
- [21] B. Sinkovic, P. D. Johnson, N. B. Brookes, A. Clarke, and N. V. Smith, *Phys. Rev. Lett.* **65**, 1647 (1990).

- [22] M. Kurahashi, X. Sun, S. Entani, and Y. Yamauchi, *Appl. Phys. Lett.* **93**, 132505 (2008).
- [23] T. Zemčík, *Czech. J. Phys.* **18**, 551 (1968).
- [24] D. G. Rancourt and J. Y. Ping, *Nucl. Instrum. Methods Phys. Res., Sect. B* **58**, 85 (1991).
- [25] H. Akai, M. Akai, S. Blügel, B. Drittler, H. Ebert, K. Terakura, R. Zeller, and P. H. Dederichs, *Prog. Theor. Phys. Suppl.* **101**, 11 (1990).
- [26] H. Akai and T. Kotani, *Hyperfine Interact.* **120–121**, 3 (1999).
- [27] M. Ogura and H. Akai, *J. Phys. Condens. Matter* **17**, 5741 (2005).
- [28] P. Dufek, P. Blaha, and K. Schwarz, *Phys. Rev. Lett.* **75**, 3545 (1995).
- [29] A. Vega, A. Rubio, L. C. Balbas, J. D. Davila, C. Demangeat, A. Mokrani, and H. Dreyssé, *J. Magn. Magn. Mater.* **104–107**, 1687 (1992).
- [30] D. Stoeffler and F. Gautier, *J. Magn. Magn. Mater.* **147**, 260 (1995).
- [31] P. Parida, B. Ganguli, and A. Mookerjee, *Superlattices Microstruct.* **86**, 173 (2015).
- [32] J. Korecki and U. Gradmann, *Phys. Rev. Lett.* **55**, 2491 (1985).
- [33] C. L. Fu and A. J. Freeman, *J. Magn. Magn. Mater.* **69**, L1 (1987).
- [34] Y. Saito, H. Uemura, and M. Uwaha, *Phys. Rev. B* **63**, 045422 (2001).